JOURNAL OF AIRCRAFT
Vol. 30, No. 6, Nov.–Dec. 1993

Aerodynamic Shape Optimization Using Sensitivity Analysis on Third-Order Euler Equations

Oktay Baysal,* Mohamed E. Eleshaky,† and Greg W. Burgreen‡
Old Dominion University, Norfolk, Virginia 23529

Previously, the authors have shown an aerodynamic optimization method with two design variables using sensitivity analysis on the first-order-accurate discretization of the Euler equations. Two advancements of this method are reported in this article. First, nonlinear fluid dynamic phenomena including flow discontinuities are better predicted by an improved flow prediction method which uses the third-order accurate discretization of the Euler equations. Using this method, the flowfield of a modified shape which generates shocks and other large gradients is predicted based on the shock-free flowfield of the original shape and without solving the flowfield equations. Secondly, every surface grid point is used as a design variable, which virtually eliminates all geometrical restrictions on the shape as it is optimized for the specified objective. This improved algorithm is demonstrated by optimizing the ramp shape of a scramjet-afterbody configuration for maximum axial thrust. Starting with totally different initial designs, virtually identical shapes are obtained as the optimum. The method is more efficient than the traditional design methods for a few reasons, which include the use of flow predictions and the elimination of a priori guessing of possible shapes from which the optimum is to be selected.

Introduction

A TYPICAL aerodynamic design optimization procedure consists of the following components: 1) the formulation of the objective function and the pertinent aerodynamic as well as geometrical constraints; 2) the definition of geometrical aerodynamic shapes; 3) the computational fluid dynamics (CFD) analysis; 4) the gradients of the objective function and the constraints with respect to the design variables (sensitivity coefficients); 5) the optimization algorithm; and 6) the gradients of the optimum design with respect to the design parameters (sensitivity derivatives).

For a particular application, the choice of methods for each of the above components influences not only the efficiency of the optimization procedure, but also the accuracy of its results. The first component of the aerodynamic design optimization procedure is case-dependent and requires a level of expertise in the field of application in question. The second component may require a significant level of experience and skill if the geometric shape is to be explicitly prescribed from a matrix of basis shapes. However, this latter requirement can almost be eliminated if a method is developed to automatically shape the aerodynamic configuration to any arbitrary geometry during the optimization process. This is one of the objectives of this article.

The third and fourth components are the dominant contributors to the computational cost as well as to the accuracy of the results. The authors have previously proposed three different methods, similar to those developed for the structural mechanics design problems, to determine the sensitivity coefficients based on the first-order accurate discretization of the Euler equations.[1] Furthermore, a first-order flow prediction method has also been developed and reported in Ref. 1. That is, given the CFD analysis for a particular configuration, this method can predict the flowfield solution for a small perturbation of the configuration at a computational cost which is equal to a small fraction of the complete CFD analysis cost.

Another objective of this article is to extend both the flow prediction method and the algorithm for determining the sensitivity coefficients to use the third-order accurate discretization of the Euler equations. The motivation is to obtain higher fidelity sensitivity coefficients and, consequently, predict more accurately nonlinear physical phenomena, which may occur in the flowfield, without performing a complete CFD analysis.

The fifth component is also a field of intense research, where many unanswered issues still exist. Such issues are beyond the objectives of this article, but rather, the approach here is to utilize the existing methods[2] in a modular manner. The authors have reported[3] an algorithm in which a proven optimization method has been coupled with a CFD analysis method,[4] a flow prediction method,[1] and a sensitivity coefficient method.[1] Furthermore, a method to determine the sensitivity derivatives of the optimum design, i.e., the sixth component, has been developed for the inviscid aerodynamics (Euler) equations and reported in Ref. 3.

The present design method is demonstrated by optimizing the ramp shape of a scramjet-afterbody configuration for maximum axial thrust. One of the reported techniques for optimizing the internal-external nozzle under consideration is the variational calculus approach combined with the method of characteristics.[5] Using this technique, the contour shapes are geometrically limited to a class of surfaces described by free parameters. A similar approach is reported[6] with potential applications for axisymmetric afterbodies; the objective and the constraints are formulated such that a minimum drag profile can be obtained analytically using the variational principles. Another way of finding the optimum is the traditional "cut-and-try" approach, which necessitates experience in prescribing the feasible classes of surfaces among which the optimum may exist. With incremented values of the design variables, this approach requires repetitive flow analyses, which are often too many for a comprehensive search, and results in prohibitive computational costs.

The aerodynamic design optimization methodology reported in Ref. 3 alleviates many of the above disadvantages.

Presented as Paper 91-1577 at the AIAA 10th Computational Fluid Dynamics Conference, Honolulu, HI, June 24–26, 1991; received Oct. 18, 1991; revision received March 9, 1993; accepted for publication March 12, 1993.

*Professor, Mechanical Engineering and Mechanics Department. Senior Member AIAA.

†Postdoctoral Fellow, Mechanical Engineering and Mechanics Department. Member AIAA.

‡Graduate Research Assistant, Mechanical Engineering and Mechanics Department. Student Member AIAA.

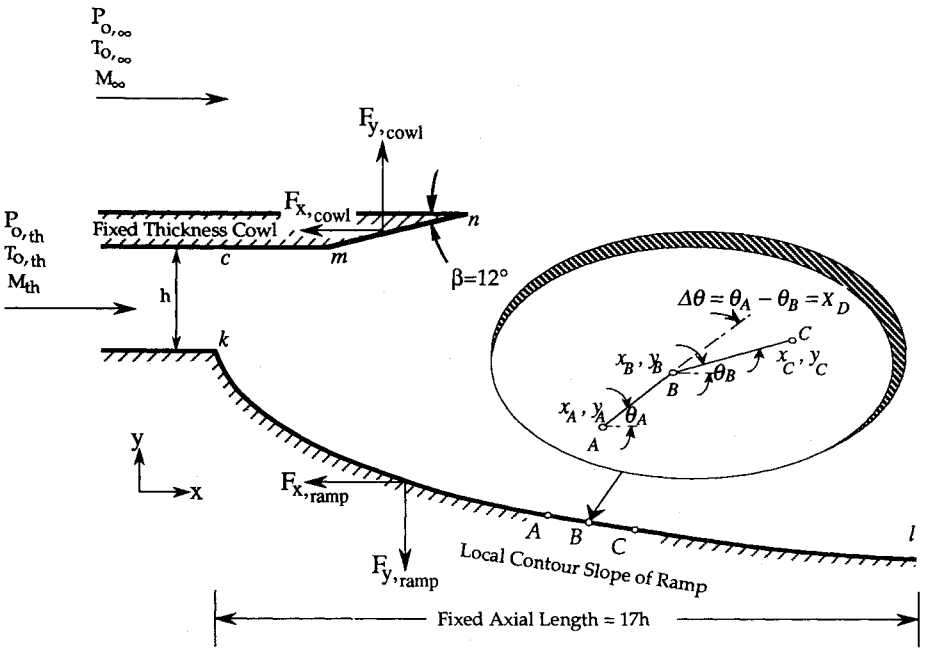

Fig. 1 Shape optimization problem. The inset depicts the surface definition by means of grid point coordinates and the relative slopes.

However, the optimum ramp and cowl shapes[3] were geometrically constrained to flat surfaces of arbitrary inclination since the number of design variables was restricted to two. The present method can change the surface to any arbitrary shape. Therefore, the first five components of the aerodynamic design optimization procedure are considered from two perspectives: 1) as they pertain to the advances in the present methodology, and 2) as they are applied to the present demonstrative example.

Optimization Problem

It is desired to determine the nozzle ramp shape which yields a maximum axial thrust force coefficient F, subject to aerodynamic and geometrical constraints, G_j (Fig. 1). For the present problem, the local contour slopes at each surface grid point are used as the design variables, $\bar{X}_D$. Mathematically, it is required to get

$$\max \quad F[\bar{Q}(\bar{X}_D), \bar{X}_D] \tag{1}$$

subject to

$$G_j[\bar{Q}(\bar{X}_D), \bar{X}_D] \leq 0, \qquad j = 1, \text{NCON} \tag{2}$$

$$\bar{X}_{D_{\text{lower}}} \leq \bar{X}_D \leq \bar{X}_{D_{\text{upper}}} \tag{3}$$

where NCON is the number of constraints, and $\bar{Q}$ is the vector of the conserved variables of the fluid flow. $\bar{X}_{D_{\text{lower}}}$ and $\bar{X}_{D_{\text{upper}}}$ are the lower and the upper bounds of the design variables.

The component of the axial thrust force due to nozzle wall shape F_{axial} is obtained by numerically integrating the pressure P over the ramp and cowl surfaces. Then it is normalized by the force associated with the inflow, which is parallel to the cowl surface. For a constant inflow Mach number M_{th}, the inflow force is centered at the midpoint of the line segment $\overline{kc}$, and its value is

$$F_{\text{inflow}} = P_{\text{th}}(1 + \gamma M_{\text{th}}^2)h \tag{4}$$

where h is the throat (th) height and γ is the ratio of the specific heats. By definition, the axial thrust force coefficient F is given[3] as

$$F = \frac{F_{\text{axial}}}{F_{\text{inflow}}} = \frac{\left(\int_k^l P_{\text{ramp}}\, dy\right) + \left(\int_m^n P_{\text{cowl}}\, dy\right)}{F_{\text{inflow}}} \tag{5}$$

This axial thrust force coefficient is subject to three aerodynamic constraints (NCON = 3). The first constraint requires that the static pressure at the ramp tip P_l remains greater than a fixed percentage of the freestream static pressure P_∞, such that maximum expansion over the ramp occurs without any reverse flow. The second and third constraints require that the static pressure at the cowl tip P_n should be within specified limits of the freestream static pressure, such that expansion waves emanating from the ramp's initial expansion do not induce any reverse flow on either the internal or external cowl surfaces.

The geometrical constraints on the configuration (Fig. 1) are chosen such that the axial length of the ramp is fixed. Also, in order to maintain an acceptably smooth aerodynamic surface, upper and lower limits of +5 deg and −5 deg, respectively, are imposed on the local contour slopes relative to their neighbors.

This nonlinear, constrained optimization problem is solved using the modified feasible directions method reported by Vanderplaats.[2] Since this optimization process requires many evaluations of the objective function and constraints before an optimum design is reached, the process can be very expensive if a CFD analysis is performed for each evaluation. In the present study, a high-fidelity flow prediction method (also called "approximate flow analysis") is performed during the one-dimensional searches of the optimization process. A complete CFD analysis is performed only when new gradients of the constraints and the objective function are needed, i.e., when the design changes substantially.

Sensitivity Coefficients

The derivative of the objective function F and constraints G_j with respect to the design variables $\bar{X}_D$, are given by

$$\nabla F \equiv \frac{\partial F}{\partial \bar{X}_D} = \left(\frac{\partial F}{\partial \bar{X}}\right)_Q + \left(\frac{\partial F}{\partial \bar{Q}}\right)^T \cdot \frac{\partial \bar{Q}}{\partial \bar{X}_D} \tag{6}$$

$$\nabla G_j \equiv \frac{\partial G_j}{\partial \bar{X}_D} = \left(\frac{\partial G_j}{\partial \bar{X}_D}\right)_Q + \left(\frac{\partial G_j}{\partial \bar{Q}}\right)^T \cdot \frac{\partial \bar{Q}}{\partial \bar{X}_D} \qquad j = 1, \text{NCON} \tag{7}$$

These derivatives have been determined in Ref. 1 for a case with two design variables and three constraint functions using two approaches: namely, the finite difference approach and the quasi-analytical or sensitivity analysis approach. In the sensitivity analysis approach, one of two methods can be used; either the direct method or the adjoint variable method. It is reported[1] that if the number of design variables (NDV) is greater than the number of adjoint vectors (NCON + 1), then the adjoint variable method is more efficient than the direct method. Since, in the present study, the number of design variables (NDV = 47) is greater than the number of adjoint vectors (NCON + 1 = 4), the adjoint variable method is selected to determine the sensitivity coefficients.

To obtain the derivatives of the flow solution in the above equations, $(\partial \bar{Q}/\partial \bar{X}_D)$, the governing equations for a two-dimensional, steady, compressible, inviscid flow of an ideal gas with constant specific heat ratios, are written in terms of the design variables

$$\bar{R}[\bar{Q}(\bar{X}_D), \bar{X}_D] = \frac{\partial \hat{f}}{\partial \xi} + \frac{\partial \hat{g}}{\partial \eta} = 0 \tag{8}$$

where $\hat{f}$ and $\hat{g}$ are the flux vectors in generalized coordinates (ξ, η).

The quasi-analytical approach[1] begins by differentiating Eq. (8) with respect to the design variables to yield the sensitivity equation

$$\left[\frac{\partial \bar{R}}{\partial \bar{Q}}\right]\left\{\frac{\partial \bar{Q}}{\partial \bar{X}_D}\right\} = -\left[\frac{\partial \bar{R}}{\partial \bar{X}_D}\right] \tag{9}$$

At this point, the adjoint variable method diverges from the direct method. First, Eq. (9) is substituted into Eqs. (6) and (7). Then, the vectors of adjoint variables $\bar{\lambda}_1$ and $\bar{\lambda}_{2j}$ are defined to satisfy the following equations:

$$\left[\frac{\partial \bar{R}}{\partial \bar{Q}}\right]^T \bar{\lambda}_1 = \frac{\partial F}{\partial \bar{Q}} \tag{10}$$

$$\left[\frac{\partial \bar{R}}{\partial \bar{Q}}\right]^T \bar{\lambda}_{2j} = \frac{\partial G_j}{\partial \bar{Q}} \qquad j = 1, \text{NCON} \tag{11}$$

Hence, Eqs. (6) and (7) are manipulated to form the following equations:

$$\frac{\partial F}{\partial \bar{X}_D} = \left(\frac{\partial F}{\partial \bar{X}_D}\right)_Q - \bar{\lambda}_1^T \left[\frac{\partial \bar{R}}{\partial \bar{X}_D}\right] \tag{12}$$

$$\frac{\partial G_j}{\partial \bar{X}_D} = \left(\frac{\partial G_j}{\partial \bar{X}_D}\right)_Q - \bar{\lambda}_{2j}^T \left[\frac{\partial \bar{R}}{\partial \bar{X}_D}\right] \qquad j = 1, \text{NCON} \tag{13}$$

The adjoint variable method requires the solution of Eqs. (10) and (11) for the adjoint variable vectors. The derivatives of F and G_j are obtained by means of Eqs. (12) and (13). It should be noticed that Eqs. (10) and (11) are independent of any differentiation with respect to $\bar{X}_D$; hence, the vectors $\bar{\lambda}_1$ and $\bar{\lambda}_{2j}$ in Eqs. (12) and (13) remain the same for all the elements of the vector $\bar{X}_D$.

Sensitivity Solution Method

In order to analyze numerically the flowfield during the optimization process, Eq. (8) is solved by a third-order accurate, implicit, upwind finite volume scheme,[7,8] where the residual is driven to zero at each point of the computational domain. Equation (8) is discretized in an upwind-biased form at an interior cell (i, j) as follows (Fig. 2):

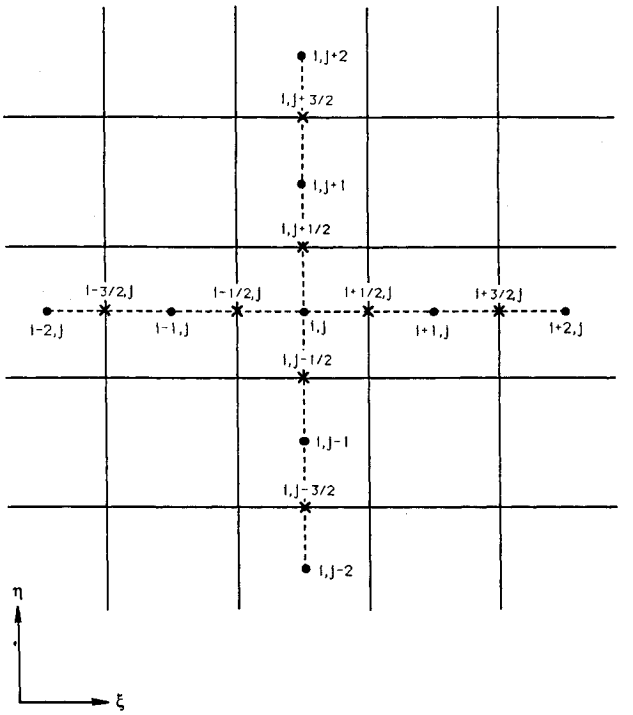

Fig. 2 Nine-point stencil of the third-order CFD scheme.

$$\begin{aligned}\bar{R}_{i,j} = {} & \hat{f}^+(\bar{Q}^-_{i+1/2,j}, M_{i+1/2,j}) - \hat{f}^+(\bar{Q}^-_{i-1/2,j}, M_{i-1/2,j}) \\ & + \hat{f}^-(\bar{Q}^+_{i+1/2,j}, M_{i+1/2,j}) - \hat{f}^-(\bar{Q}^+_{i-1/2,j}, M_{i-1/2,j}) \\ & + \hat{g}^+(\bar{Q}^-_{i,j+1/2}, M_{i,j+1/2}) - \hat{g}^+(\bar{Q}^-_{i,j-1/2}, M_{i,j-1/2}) \\ & + \hat{g}^-(\bar{Q}^+_{i,j+1/2}, M_{i,j+1/2}) - \hat{g}^-(\bar{Q}^+_{i,j-1/2}, M_{i,j-1/2})\end{aligned} \tag{14}$$

where $\hat{f}^+$, $\hat{f}^-$, $\hat{g}^+$, and $\hat{g}^-$ are the operator-split inviscid fluxes. M represents the projected surface areas for these flux vectors and is associated with the coordinate transformation metrics. The values of $\bar{Q}^{\pm}_{i\pm1/2,j}$ and $\bar{Q}^{\pm}_{i,j\pm1/2}$ are determined using the upwind-biased MUSCL-type scheme with the van Albada limiter.[7] For example, these expressions for the $(i + \frac{1}{2}, j)$ face are given by

$$\bar{Q}^-_{i+1/2,j} = \bar{Q}_{i,j} + \{(S/4)[(1 - \kappa S)\Delta_- + (1 + \kappa S)\Delta_+]\}_{i,j} \tag{15}$$

$$\bar{Q}^+_{i+1/2,j} = \bar{Q}_{i+1,j} - \{(S/4)[(1 - \kappa S)\Delta_+ + (1 + \kappa S)\Delta_-]\}_{i+1,j} \tag{16}$$

where

$$S = \frac{2\Delta_+\Delta_- + \varepsilon}{(\Delta_+)^2 + (\Delta_-)^2 + \varepsilon} \tag{17}$$

$$\Delta_+ = \bar{Q}_{i+1,j} - \bar{Q}_{i,j}, \qquad \Delta_- = \bar{Q}_{i,j} - \bar{Q}_{i-1,j} \tag{18}$$

Different schemes can be obtained by varying the values of κ. For example, κ values of $(\frac{1}{3})$ and (-1) correspond to the third-order upwind-biased and the second-order fully upwind schemes, respectively. By setting $S = 0$, the first-order upwind scheme used in Refs. 1 and 3 can be recovered. To prevent division by zero in regions of null gradients, the small value of $\varepsilon = 10^{-6}$ is included in Eq. (17).

The left side of Eq. (9) is evaluated by differentiating the upwind discretized form given by Eq. (14) for an interior cell (i, j) with respect to $(\bar{Q}^{\mp}_{i\pm 1/2,j\pm 1/2})$ as follows:

$$[\text{LS of Eq. (9)}]_{i,j} = \frac{\partial \bar{R}_{i,j}}{\partial \bar{Q}^{-}_{i+1/2,j}} \frac{\partial \bar{Q}^{-}_{i+1/2,j}}{\partial \bar{X}_D} + \frac{\partial \bar{R}_{i,j}}{\partial \bar{Q}^{+}_{i+1/2,j}} \frac{\partial \bar{Q}^{+}_{i+1/2,j}}{\partial \bar{X}_D} + \frac{\partial \bar{R}_{i,j}}{\partial \bar{Q}^{+}_{i-1/2,j}} \frac{\partial \bar{Q}^{+}_{i-1/2,j}}{\partial \bar{X}_D} + \frac{\partial \bar{R}_{i,j}}{\partial \bar{Q}^{-}_{i-1/2,j}} \frac{\partial \bar{Q}^{-}_{i-1/2,j}}{\partial \bar{X}_D} + \frac{\partial \bar{R}_{i,j}}{\partial \bar{Q}^{-}_{i,j+1/2}} \frac{\partial \bar{Q}^{-}_{i,j+1/2}}{\partial \bar{X}_D} + \frac{\partial \bar{R}_{i,j}}{\partial \bar{Q}^{-}_{i,j-1/2}} \frac{\partial \bar{Q}^{-}_{i,j-1/2}}{\partial \bar{X}_D} + \frac{\partial \bar{R}_{i,j}}{\partial \bar{Q}^{+}_{i,j+1/2}} \frac{\partial \bar{Q}^{+}_{i,j+1/2}}{\partial \bar{X}_D} + \frac{\partial \bar{R}_{i,j}}{\partial \bar{Q}^{+}_{i,j-1/2}} \frac{\partial \bar{Q}^{+}_{i,j-1/2}}{\partial \bar{X}_D} \tag{19}$$

The terms $\partial \bar{Q}^{\mp}_{i\pm 1/2,j}/\partial \bar{X}_D$, $\partial \bar{Q}^{\mp}_{i,j\pm 1/2}/\partial \bar{X}_D$, in Eq. (19) are functions of $\partial \bar{Q}_{i\pm 2,j}/\partial \bar{X}_D$, $\partial \bar{Q}_{i\pm 1,j}/\partial \bar{X}_D$, $\partial \bar{Q}_{i,j}/\partial \bar{X}_D$, $\partial \bar{Q}_{i,j\pm 1}/\partial \bar{X}_D$, and $\partial \bar{Q}^{+}_{i,j\pm 2}/\partial \bar{X}_D$ by means of Eqs. (15–18). Then, Eq. (19) can be rewritten as

$$[\text{LS of Eq. (9)}]_{i,j} = \bar{D} \frac{\partial \bar{Q}_{i-2,j}}{\partial \bar{X}_D} + \bar{A} \frac{\partial \bar{Q}_{i-1,j}}{\partial \bar{X}_D} + \bar{B} \frac{\partial \bar{Q}_{i,j}}{\partial \bar{X}_D} + \bar{C} \frac{\partial \bar{Q}_{i+1,j}}{\partial \bar{X}_D} + \bar{E} \frac{\partial \bar{Q}_{i+2,j}}{\partial \bar{X}_D} + \bar{H} \frac{\partial \bar{Q}_{i,j-2}}{\partial \bar{X}_D} + \bar{F} \frac{\partial \bar{Q}_{i,j-1}}{\partial \bar{X}_D} + \bar{G} \frac{\partial \bar{Q}_{i,j+1}}{\partial \bar{X}_D} + \bar{I} \frac{\partial \bar{Q}_{i,j+2}}{\partial \bar{X}_D} \tag{20}$$

It is observed that the above equation is characterized by a nine-point stencil (Fig. 2), which is a consequence of the third-order discretization of Eq. (14). The coefficients $\bar{A}$ through $\bar{I}$ in Eq. (20) are 4×4 block matrices which are functions of the flux Jacobians in Eq. (19). These flux Jacobians are available from the solver of the flow equations. Hence, only a few computations are needed to assemble the coefficient matrix $[\partial \bar{R}/\partial \bar{Q}]$ in Eq. (9). However, it is necessary to revise the residual [Eq. (14)] and the coefficient matrix at the boundary cells to include the implicit boundary conditions.[9]

The coefficient matrix of Eq. (9) is block-banded with nine nonzero diagonals, due to the nine-point stencil. For a two-dimensional computational domain with I cells in the ξ direction, and J cells in the η direction, the matrix dimension is $(4IJ)$. The third-order upwind discretization of the governing equations yields a coefficient matrix with a half-bandwidth of $(8J + 3)$ or $(8I + 3)$. The computational grid (Fig. 3) used here has 52×40 cells, which produces a coefficient matrix requiring approximately 2.31 gigabytes of computer memory. Hence, to reduce this enormous memory requirement, diagonal storage of banded matrices and preferred ordering of the unknowns are used.[1]

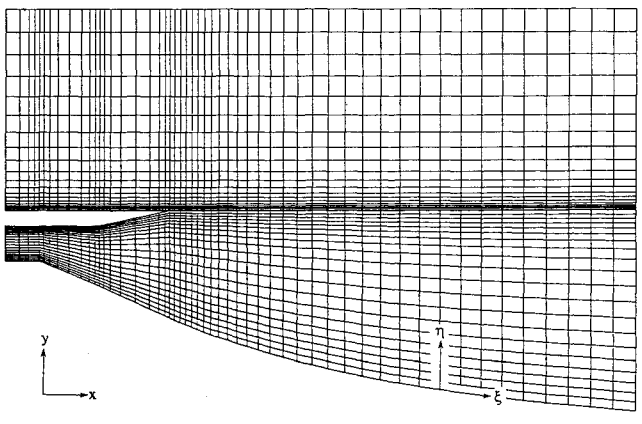

Fig. 3 Representative computational grid for the nozzle-afterbody flowfield.

The right side of Eq. (9) is evaluated by differentiating the upwind discretized form given by Eq. (14) for an interior cell (i, j) with respect to the design variables, $\bar{X}_D$, as follows:

$$\frac{\partial \bar{R}_{i,j}}{\partial \bar{X}_D} = \frac{\partial \hat{f}^{+}_{i,j}}{\partial (M_{i+1/2,j})} \frac{\partial (M_{i+1/2,j})}{\partial \bar{X}_D} - \frac{\partial \hat{f}^{-}_{i,j}}{\partial (M_{i-1/2,j})} \frac{\partial (M_{i-1/2,j})}{\partial \bar{X}_D} + \frac{\partial \hat{g}^{+}_{i,j}}{\partial (M_{i,j+1/2})} \frac{\partial (M_{i,j+1/2})}{\partial \bar{X}_D} - \frac{\partial \hat{g}^{-}_{i,j}}{\partial (M_{i,j-1/2})} \frac{\partial (M_{i,j-1/2})}{\partial \bar{X}_D} - \frac{\partial \hat{f}^{+}_{i-1,j}}{\partial (M_{i-1/2,j})} \frac{\partial (M_{i-1/2})}{\partial \bar{X}_D} + \frac{\partial \hat{f}^{-}_{i+1,j}}{\partial (M_{i+1/2,j})} \frac{\partial (M_{i+1/2})}{\partial \bar{X}_D} - \frac{\partial \hat{g}^{+}_{i,j-1}}{\partial (M_{i,j-1/2})} \frac{\partial (M_{i,j-1/2,j})}{\partial \bar{X}_D} + \frac{\partial \hat{g}^{+}_{i,j+1}}{\partial (M_{i,j+1/2})} \frac{\partial (M_{i,j+1/2,j})}{\partial \bar{X}_D} \tag{21}$$

As seen from Eq. (21), $[\partial \bar{R}/\partial \bar{X}_D]$ depends on the derivatives of the projected surface areas (M) with respect to the design variables. If an explicit analytical expression for $M = M(\bar{X}_D)$ exists, then this differentiation is straightforward. Otherwise, a finite difference approximation for $\partial M/\partial \bar{X}_D$ with a small step size $\Delta \bar{X}_D$ can be used. Implied here is the dependence of the grid on the design variables. That is, the grid point coordinates can be analytically related to the parameters defining the surface being redesigned. This so-called "grid sensitivity" relationship and the regeneration of the grid during the optimization process are further explained in Refs. 9 and 10.

The right sides of Eqs. (10) and (11) are obtained by differentiating Eqs. (2) and (5) with respect to the vector of conserved variables of the flow, $\bar{Q}$. The solution of the sets of linear algebraic Eqs. (9–11) are achieved by using the Gauss elimination method.

Flow Prediction Method

An approximate flow analysis method has been introduced in Refs. 1–3 to predict a flowfield solution of a perturbed shape $(\bar{X}^{*}_D + \Delta \bar{X}_D)$ using the flowfield solution of an initially unperturbed shape $(\bar{X}^{*}_D)$. This method is based on a Taylor series expansion of the vector of conserved variables $\bar{Q}(\bar{X}^{*}_D + \Delta \bar{X}_D)$ about $\bar{Q}(\bar{X}^{*}_D)$ as follows:

$$\bar{Q}(\bar{X}^{*}_D + \Delta \bar{X}_D) = \bar{Q}(\bar{X}^{*}_D) + \left(\frac{\partial \bar{Q}}{\partial \bar{X}_D}\right)_{\bar{X}_D = \bar{X}^{*}_D} \Delta \bar{X}_D + \cdots \tag{22}$$

Substituting Eq. (9) into (22) results in

$$\left\{\frac{\partial \bar{R}[\bar{Q}(\bar{X}^{*}_D), \bar{X}^{*}_D]}{\partial \bar{Q}}\right\} \Delta \bar{Q} = -\left\{\frac{\partial \bar{R}[\bar{Q}(\bar{X}^{*}_D), \bar{X}^{*}_D]}{\partial \bar{X}_D}\right\} \Delta \bar{X}_D \tag{23}$$

where

$$\Delta \bar{Q} = \bar{Q}(\bar{X}^{*}_D + \Delta \bar{X}_D) - \bar{Q}(\bar{X}^{*}_D) \tag{24}$$

Equation (23) explicitly gives the changes in $\bar{Q}$ due to the changes in $\Delta \bar{X}_D$. In other words, the flowfield solution $\bar{Q}(\bar{X}^{*}_D + \Delta \bar{X}_D)$ associated with the perturbed shape, $(\bar{X}^{*}_D + \Delta \bar{X}_D)$, is predicted using Eq. (23), which is based on the given flowfield solution, $\bar{Q}(\bar{X}^{*}_D)$, associated with the original shape $(\bar{X}^{*}_D)$. Herein the term "prediction" is used when the flowfield is predicted using Eq. (23), and the term "analysis" is used when the complete governing equations (Eq. 8) are solved with the CFD algorithm. It should be noted that Eq. (23) represents a linear system of algebraic equations regardless of the linearity or nonlinearity of the flowfield governing equations.

To investigate the capability of predicting flowfield discontinuities, which can be treated as large gradients by CFD analysis methods, using this method, the three-dimensional space of Fig. 4 is considered. The CFD solution $\bar{Q}$ is represented as a function of one design variable, (X_{D_1}) and one of the physical coordinates, x. Two values of the design variable are considered. At the first value, $(X^0_{D_1})$, the function is continuous. Whereas, at the perturbed value, $(X^*_{D_1})$, a steep gradient is assumed to occur in the $(Q\text{-}x)$ plane. Furthermore, the values of $\bar{Q}$ at points A and A' are assumed to be equal (i.e., $\partial \bar{Q}_A/\partial X_{D_1} = 0$). Whereas, the values of $\bar{Q}$ at points C and C' are not equal to each other due to the steep gradient in $\bar{Q}(x)|_{X_{D_1}}$. Now, if $\bar{Q}$ at point C is expressed in terms of (X_{D_1}), the resulting functional relationship $\bar{Q}_C(X_{D_1})$, whether it is linear or not, should always be continuous. Otherwise, the gradient of the flowfield solution at this point (i.e., $\partial \bar{Q}_C/\partial X_{D_1}$) will not exist, and consequently, the optimization problem cannot be unique. Therefore, if a shock, which is usually captured as steep but continuous gradient, exists in the flowfield, the above prediction method [Eq. (23)] should predict it accurately so long as a sufficiently small $\Delta \bar{X}_D$ is used.

An immediate improvement of the flow prediction method is its extension to a "multilevel prediction," which is accomplished as follows. Similar to Eq. (22), performing a first-order Taylor series expansion of $\bar{Q}[\bar{X}^*_D + \Delta\bar{X}^{(1)}_D + \Delta\bar{X}^{(2)}_D]$ about $\bar{Q}[\bar{X}^*_D + \Delta\bar{X}^{(1)}_D]$, gives

$$\bar{Q}[\bar{X}^*_D + \Delta\bar{X}^{(1)}_D + \Delta\bar{X}^{(2)}_D] = \bar{Q}[\bar{X}^*_D + \Delta\bar{X}^{(1)}_D] + \left(\frac{\partial \bar{Q}}{\partial \bar{X}_D}\right)_{\bar{X}_D = \bar{X}^*_D + \Delta\bar{X}^{(1)}_D} \Delta\bar{X}^{(2)}_D + \cdots \tag{25}$$

where $\Delta\bar{X}^{(2)}_D$ is the sequent design variable perturbation of the initial perturbation, $\Delta\bar{X}^{(1)}_D$. Then, performing an operation similar to that of Eq. (23), a second level flowfield prediction analogous to Eq. (24) is obtained

$$\bar{Q}[\bar{X}^*_D + \Delta\bar{X}^{(1)}_D + \Delta\bar{X}^{(2)}_D] \simeq \bar{Q}[\bar{X}^*_D + \bar{X}^{(1)}_D] + \Delta\bar{Q}^{(2)} \tag{26}$$

where $\bar{Q}[\bar{X}^*_D + \Delta\bar{X}^{*(1)}_D]$ is obtained by Eq. (24). It should be noted that $\partial\bar{Q}/\partial\bar{X}_D$ in Eq. (25) [or, more accurately, $\partial\bar{R}/\partial\bar{Q}$ and $\partial\bar{R}/\partial\bar{X}_D$ as in Eq. (23)] is based on the predicted flowfield $\bar{Q}[\bar{X}^*_D + \Delta\bar{X}^{(1)}_D]$. This procedure allows flowfield solutions to be progressively "built up" from previous predictions, all of which have the common genesis of a single initial CFD analysis solution. Thus, a flowfield solution for a complex final shape may be obtained through a multilevel prediction based on incremental design variable perturbations. Otherwise, a grossly erroneous prediction may be produced if an equivalent single large perturbation is attempted.

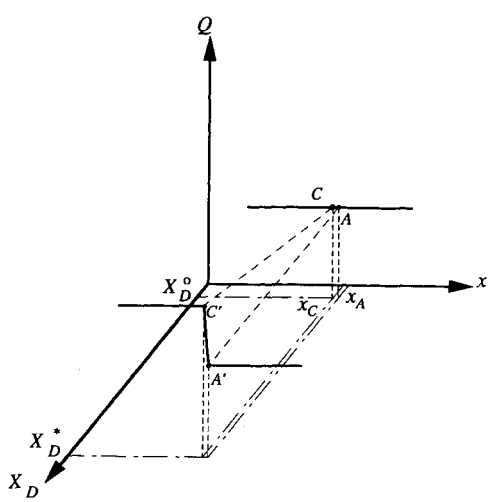

Fig. 4 Flow variable dependence on a Cartesian coordinate and a design variable in the presence of a shock: a simplified illustration.

Due to the truncation error of the first-order Taylor series, the flow prediction is certainly less accurate than the flow analysis. Consequently, it is natural to question the quality and accuracy of the flowfield predictions of Eqs. (22) and (25). This issue will be addressed in the next section. However, obtaining a flowfield prediction costs only a small fraction of solving Eq. (8). Therefore, by using the flowfield prediction method, significant time savings may be realized at the expense of some accuracy.

Results and Discussion

The upstream flow conditions, which are kept constant during the optimization process, are

External flow	Internal flow
$M_\infty = 6$	$M_{\text{th}} = 1.665$
$T_{0,\infty} = 885°\text{R}$	$T_{0,\text{th}} = 610°\text{R}$
$P_{0,\infty} = 51{,}984$ psf	$P_{0,\text{th}} = 3{,}960$ psf

where T_0 and P_0 are the total temperature and the total pressure, respectively. The throat height of the internal nozzle is 0.05 ft. All the solid walls are assumed to be adiabatic. The cowl angle, $\beta = 12$ deg, is kept constant.

The results are presented in two subsections. The flow prediction method using the third-order discretized Euler equations is examined in the first subsection. Presented in the second subsection are the demonstrative examples for the shape optimization method.

Flow Prediction Method Results

Initially, the governing equations of the flow are solved to obtain the solution for a flat ramp surface at $\theta = 0$ deg (cf. Fig. 5a). Then, a compression corner is formed at 38% length from the ramp corner by deflecting the surface at an angle θ from the ramp's surface. CFD analyses are performed for three different deflections where θ is equal to 2.5, 5, and 10 deg, respectively. The flowfields for the same θ values are then predicted using Eq. (22) based on the undeflected ($\theta = 0$ deg) flat ramp surface analysis. In other words, the $\theta = 0$ deg configuration is denoted by $(\bar{X}^*_D)$ in Eq. (22), and any one of the $\theta \neq 0$-deg configurations is denoted by $(\bar{X}^*_D + \Delta\bar{X}_D)$.

The pressure coefficient distributions along the ramp surface for the initial solution, CFD analyses, and predicted solutions are shown in Fig. 5b. The large gradient due to the compression is observed to be well predicted, especially for the smaller θ values, i.e., the smaller design variable perturbations. As expected, discrepancies begin to appear for the larger θ values. Thus, it is concluded that the prediction method's accuracy, due to truncation error, is dependent on the perturbation size $\Delta\bar{X}^*_D$. Unacceptable solutions are predicted if the perturbation size becomes too large.

The success of the prediction method for the off-surface flow is assessed by examining the flow structure over the ramp. Shown in Fig. 5c are the density contours of the unperturbed ramp shape. The salient features of the flow are the centered expansion fans at the lower and upper throat corners and a shear layer separating the external flow and the internal jet flow. Compared in Fig. 5d are the CFD analysis and the predicted solution for $\theta = 5$-deg deflection. The angle and strength of the compression wave are predicted very well. This indicates the capability of the prediction method to correctly model the characteristic wave propagation of the supersonic flow and, in turn, to represent accurately the flow physics for small design perturbations.

To demonstrate the effectiveness and accuracy of a multilevel prediction method [Eq. (25)], the following case is

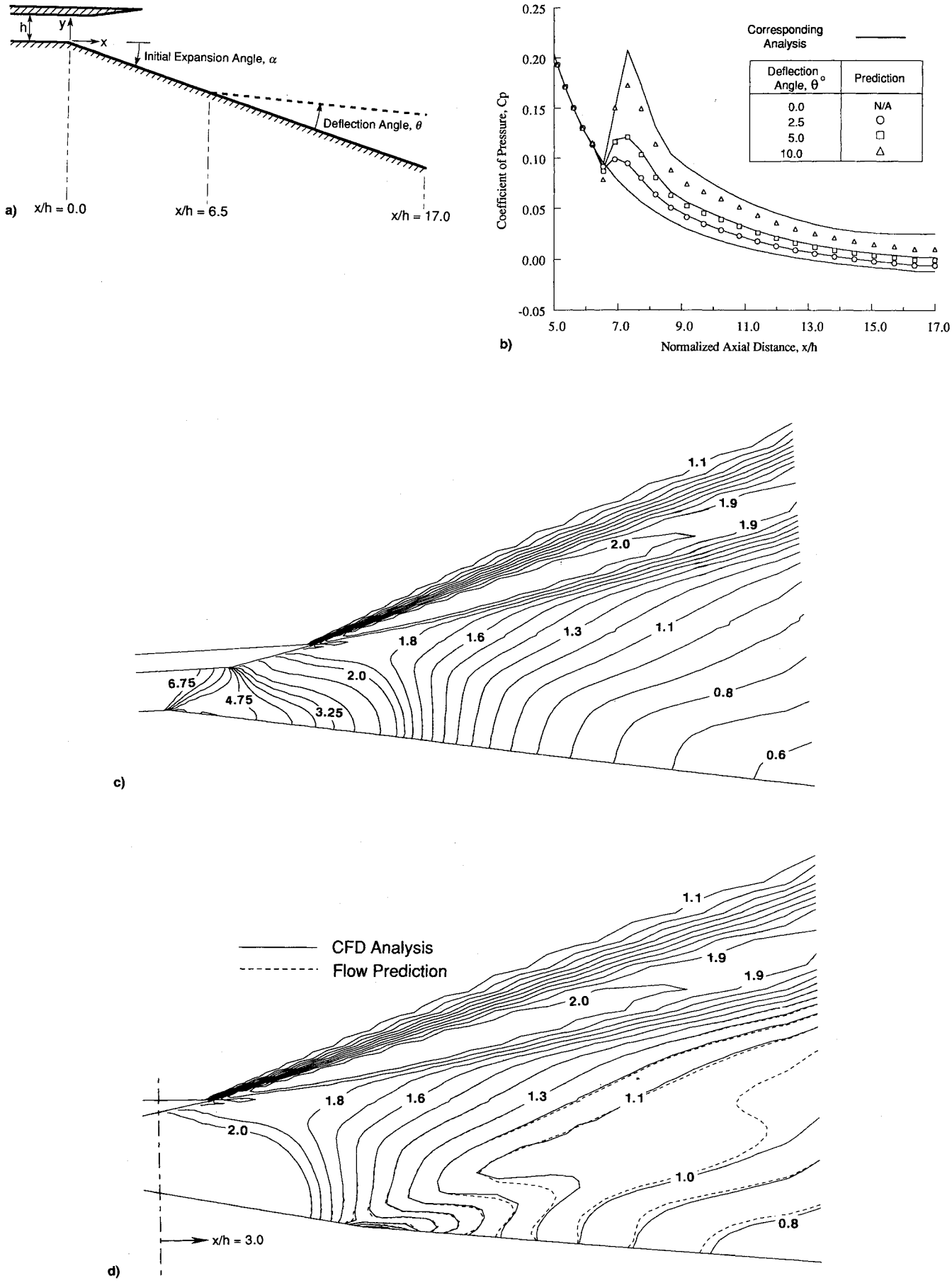

Fig. 5 Demonstrative problem for the flowfield prediction method: a) a compression corner placed on a nozzle-afterbody ramp; b) pressure coefficient distributions along the ramp with different deflection angles; c) density contours of the nozzle-afterbody flowfield without a deflection; and d) comparison of density contours for θ = 5-deg deflection on the ramp surface.

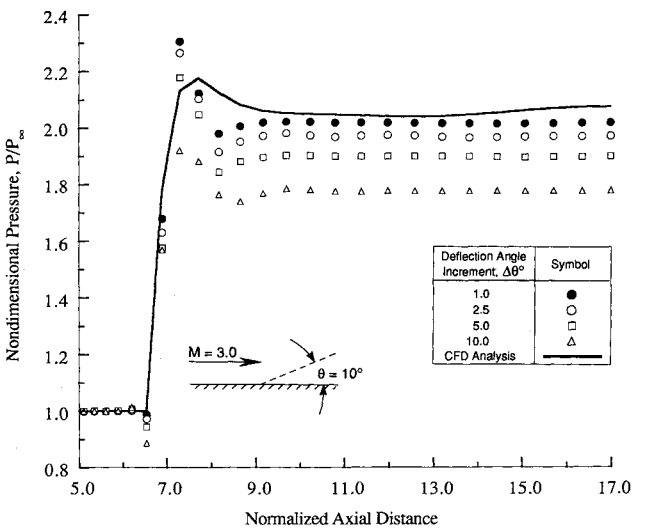

Fig. 6 Pressure coefficient distributions for Mach 3 flow past a flat plate with 10-deg deflection obtained by using different increments.

briefly examined. Consider a flat plate initially in uniform inviscid flow at Mach 3. Based on this initial condition, the flowfield is predicted for a $\theta = 10$-deg surface deflection using the multilevel prediction and various incremental deflection sizes: namely, 1-, 2.5-, 5-, and 10-deg increments. A comparison of the predicted pressure coefficient distributions along the 10-deg deflected surface with its CFD solution is shown in Fig. 6. As observed from this figure, the results improve progressively with decreasing incremental deflection sizes. Moreover, a flowfield discontinuity (shock) is predicted based on a flow which does not have that physical phenomenon (shock free). Thus, a multilevel prediction is shown to accurately predict the flowfield of a largely deformed shape, provided that the final shape is attained through a sequence of sufficiently small incremental shape changes.

Aerodynamic Shape Optimization Procedure Results

Three different and arbitrary shapes are chosen as the initial design shapes for the ramp: namely, a flat ramp surface at $\alpha = 10$ deg (case 1), a concave surface (case 2), and a convex surface (case 3). For the concave shape, the slope of the ramp's initial expansion is $\alpha = 35$ deg, and the relative slope of each sequent downstream segment is $\Delta\theta = +0.5$ deg. Similarly, for the convex shape, the initial slope is $\alpha = 23.5$ deg, and the relative slope of each downstream segment is $\Delta\theta = -0.2$ deg. The reason for starting the optimization from three different initial shapes is to determine how close the resulting optimized ramp shapes would be to each other. Ideally, the optimum values of the objective function should be identical and the optimum shapes should be fairly close to each other irrespective of their initial shapes; so that the designer using this method can start with any shape that may be convenient.

Presented in Fig. 7 are the evolutions of two of the ramp shapes during their optimization processes. For each case, the ramp's initial expansion point and axial length are the only fixed geometrical parameters. During the optimization process, the intermediate shapes (denoted by increasing iteration numbers) systematically approach the final optimum shape. For example, the initial flat ramp surface of case 1 (Fig. 7a) changes to a concave shape at the first iteration and, as the optimization process continues, its concavity increases. After the second design iteration, the slope of the ramp's initial expansion changes little as compared to that of the ramp tip. This means that no significant increases in the expansion rate at the ramp corner occurs after the second iteration; the subsequent shapes tend to recompress the flow. However, the opposite occurs in case 2 (Fig. 7b), where the shape concavity

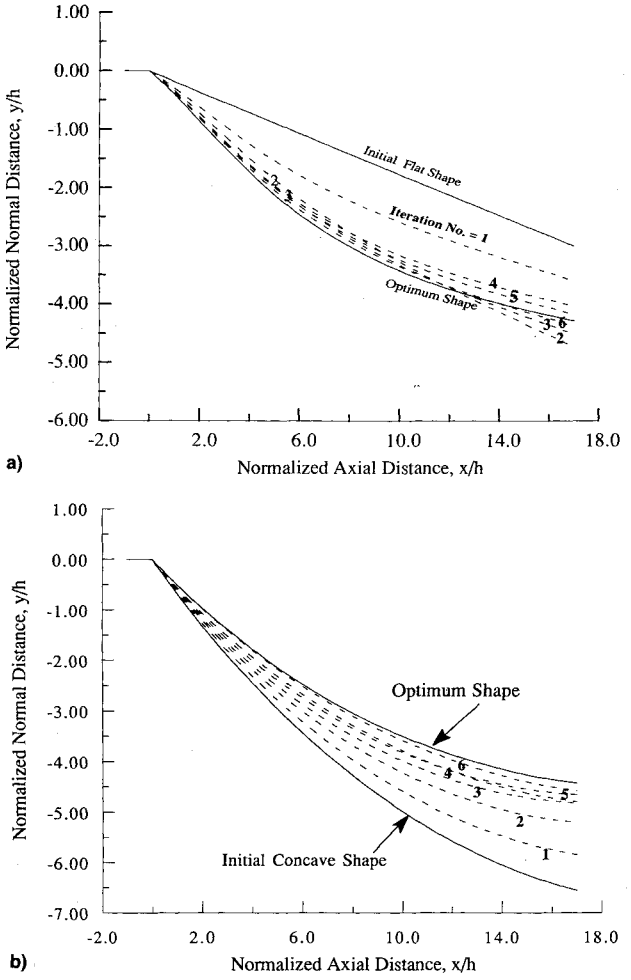

Fig. 7 Evolution of the ramp shape during the shape optimization process: a) case 1—flat initial shape; b) case 2—concave initial shape.

decreases during the last three design iterations. Shown in Fig. 8 are the comparisons of the optimum shapes along with their initial shapes. The optimum shapes are almost identical for 70% of the surface, but display a small difference towards the tip. It can be seen that the final shapes of cases 2 and 3 are nearly indistinguishable, and that of case 1 differs only towards the tip.

Plotted in Fig. 9 are the histories of the objective functions, F, during the optimization process. All three cases converge to an optimum F value within 14 optimization iterations. Cases 1 and 3 have identical optimum F values to the fourth significant digit, and that of case 2 differs from them by less than 0.5%.

The coefficient of thrust for each shape is an integrated value of the local flow quantity, C_p. To study the local effects over the optimum shape, the surface pressure coefficient distributions of all three shapes are plotted in Fig. 10. Again, the initial distributions are vastly different as deliberately chosen. The optimum distributions are not identical but very close to each other. It appears that the difference between the optimum C_p distributions can be explained in terms of the initial expansion strength of each ramp shape. For example, case 2 has the largest expansion at the corner, then it recompresses more downstream to match the expansion of the other cases. From Figures 8 and 10, it is observed that any small difference in the ramp initial angle affects the initial centered expansion significantly. Hence, obtaining truly identical optimal shapes is highly unlikely. Nevertheless, the results of all cases are very close to each other.

The effect of the shape optimization on the interior flowfield is just as pronounced as it is on the surface properties. The Mach number contours of both initial and optimum con-

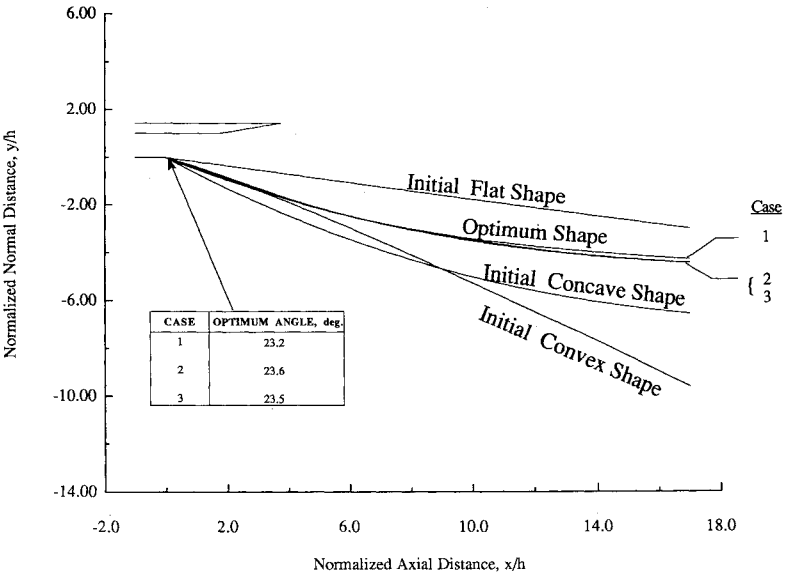

Fig. 8 Comparison of the final optimized ramp shapes.

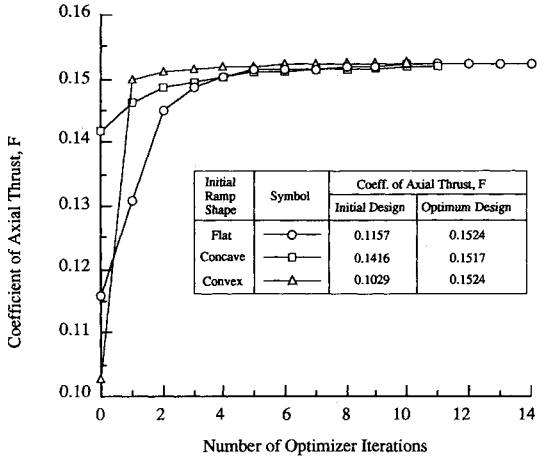

Fig. 9 Optimization history of the objective function.

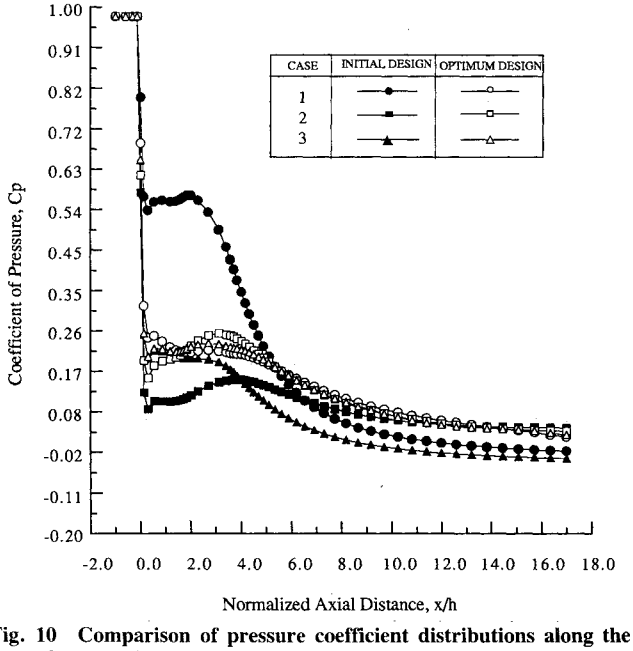

Fig. 10 Comparison of pressure coefficient distributions along the ramp for three initial and optimum shapes.

figurations of case 1 are presented in Fig. 11. The expansion patterns are significantly different. The rate of expansion is much higher inside the nozzle for the optimum shape (Fig. 11b), which results in a higher Mach number and less underexpanded jet at the nozzle exit plane. The consequence of this is evidenced in the shear layer, which becomes thinner and has a smaller angle with the horizontal for the optimum shape. Also, the expansion along the external part of the nozzle ramp is no longer predominantly in the streamwise direction, but a significant portion is in the normal direction. This indicates that cancellation of the cowl corner centered-expansion waves occurs at the optimized ramp surface, which is a characteristic feature of bell-type nozzles.

The computational time for each one of the shape optimization cases is about 7 h on the CRAY-YMP of numerical aerodynamic simulation (NAS) of NASA. For case 1, for example, 180 evaluations of the objective function are required over the course of 14 optimization iterations. At the end of each iteration, there is a CFD analysis accompanied with the objective function evaluation for the new improved shape. That is, a CFD analysis is performed 14 times, whereas, a flow prediction is performed 166 times. For the present cases, the computational cost of a flow prediction is about an order of magnitude less than that of an analysis. Hence, the aerodynamic optimization procedure becomes more efficient by employing the present flow prediction method. These numbers can vary from one case to the other depending on case related factors and algorithmic considerations. This point is further investigated in Refs. 9 and 10, resulting in significant efficiency improvements. Furthermore, this method has recently been extended for the thin-layer Navier-Stokes equations and used to optimize the shape of a transonic airfoil.[11]

Conclusions

To replace most of the repetitive flow analyses required in any aerodynamic optimization procedure, an improved flowfield prediction method has been developed. This method is used to improve the efficiency of the optimization procedure.

The flow prediction method is demonstrated by predicting the flowfield of a modified shape which generates fluid dynamic phenomena such as shocks. The predicted flow is based on the shock-free flowfield of the initial shape. The results compare very well with those obtained by performing complete CFD analyses for the same modified shapes. As expected, discrepancies between these results start to emerge and grow when large shape perturbation steps are used. Additionally, the capability of using the flow prediction method to predict flowfields of successively modified shapes, without

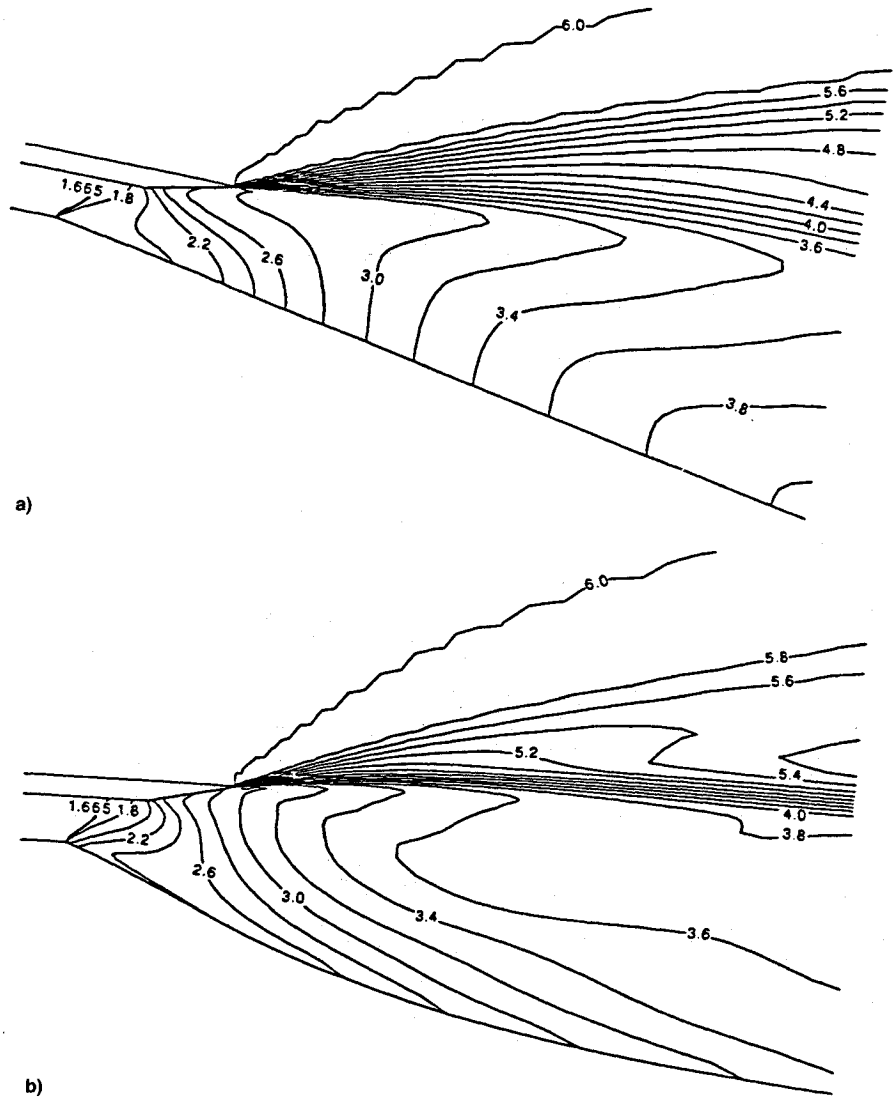

Fig. 11 Mach number contours: a) initial flat ramp shape and b) optimized ramp shape.

requiring intermediate CFD analyses, is successfully demonstrated.

The present shape optimization method is demonstrated by optimizing an internal-external nozzle shape to yield a maximum axial thrust. Although this demonstrative example is started initially from three different arbitrary designs, virtually the same optimum shape is obtained. This indicates the capability of obtaining an optimum shape with minimal dependence on the initial shape. The factors contributing to this end include the fact that the present method is not limited to any class of surfaces and, also, the accuracy and robustness of the flow prediction method.

Acknowledgments

This research is supported by NASA Langley Research Center under Grant NAG-1-1188. The technical monitor is David S. Miller.

References

[1]Baysal, O., and Eleshaky, M. E., "Aerodynamic Sensitivity Analysis Methods for the Compressible Euler Equations," *Journal of Fluids Engineering*, Vol. 113, No. 4, 1991, pp. 681–688.

[2]Vanderplaats, G. N., "ADS—A Fortran Program for Automated Design Synthesis," NASA CR 177985, Sept. 1985.

[3]Baysal, O., and Eleshaky, M. E., "Aerodynamic Design Optimization Using Sensitivity Analysis and Computational Fluid Dynamics," *AIAA Journal*, Vol. 30, No. 3, 1992, pp. 718–725.

[4]Baysal, O., Eleshaky, M. E., and Engelund, W. C., "Computations of Multispecies Mixing Between Scramjet Nozzle Flow and Hypersonic Freestream," *Journal of Propulsion and Power*, Vol. 8, No. 2, 1992, pp. 500–506.

[5]Doty, J. H., Thompson, H. D., and Hoffman, J. D., "Optimum Thrust Two-Dimensional NASP Nozzle Study," National Aero-Space Plane Program CR-1069, Wright-Patterson AFB, OH, 1989.

[6]Shmyglevskii, Y. D., "On Minimal Afterbody Drag," *Mekhanika Zhidkosti i Gaza*, Vol. 1, No. 5, 1966, pp. 102–104; see also *Fluid Dynamics*—Soviet Research.

[7]Anderson, W. K., Thomas, J. L., and Van Leer, B., "A Comparison of Finite Volume Flux Vector Splittings for the Euler Equations," AIAA Paper 85-0122, Jan. 1985.

[8]Baysal, O., Fouladi, K., and Lessard, V. R., "Multigrid and Upwind Viscous Flow Solver on 3-D Overlapped and Embedded Grids," *AIAA Journal*, Vol. 29, No. 4, 1991, pp. 903–910.

[9]Eleshaky, M. E., "A Computational Aerodynamic Design Optimization Method Using Sensitivity Analysis," Ph.D. Dissertation, Old Dominion Univ., Norfolk, VA, 1992, pp. 95–98, 207–209.

[10]Burgreen, G. W., Baysal, O., and Eleshaky, M. E., "Improving the Efficiency of Aerodynamic Optimization Procedures," *Proceedings of 4th AIAA/USAF/NASA/OAI Symposium on Multidisciplinary Analysis and Optimization*, Cleveland, OH, Sept. 1992, pp. 87–97 (AIAA Paper 92-4697 CP).

[11]Eleshaky, M. E., and Baysal, O., "Airfoil Shape Optimization Using Sensitivity Analysis on Viscous Flow Equations," *Journal of Fluids Engineering*, Vol. 115, No. 1, 1993, pp. 75–84.